Applied Catalysis A, General 714 (2026) 120846

Contents lists available at ScienceDirect

Applied Catalysis A, General

journal homepage: www.elsevier.com/locate/apcata

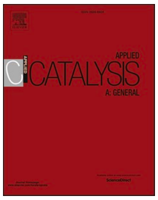

Crystallographic location of active sites in ZSM-5 determined by quantitative STEM

Ping-Luen Baron Ho [a,b,*,1], Christopher Foo [a,c,1], Xiting Yue [d,e,1], Tsz-Woon Benedict Lo [d], Wei-Che Lin [a], Tsai-Fu Chung [f], Yung-Kang Peng [e], Guangchao Li [d,**], Shik Chi Edman Tsang [a,d,2]

[a] *Wolfson Catalysis Centre, Department of Chemistry, University of Oxford, Oxford OX1 3QR, United Kingdom*
[b] *Department of Materials and London Centre for Nanotechnology, Imperial College London, London SW7 2AZ, United Kingdom*
[c] *Diamond Light Source, Didcot OX11 0DE, United Kingdom*
[d] *Department of Applied Biology and Chemical Technology, The Hong Kong Polytechnic University, 999077, Hong Kong Special Administrative Region of China*
[e] *Department of Chemistry, City University of Hong Kong, Kowloon 999077, Hong Kong Special Administrative Region of China*
[f] *Department of Materials Science and Engineering, National Yang Ming Chiao Tung University, Hsinchu 300093, Taiwan*

ARTICLE INFO

Keywords:
ZSM-5
Al site-selective distribution
Molecular probe
Brønsted acid sites in zeolites, Scanning transmission electron microscopy

ABSTRACT

In aluminosilicate zeolites, the atomic-scale insights into catalytic performance are tied to Brønsted acid sites (BASs), the primary active sites generated by the substitution of aluminum (Al) for silicon (Si) in the tetrahedral framework, with a proton (H^+) compensating for the resultant charge imbalance. The profound influence of Al distribution on BAS density, spatial arrangement, and acidity is well established. Yet, the precise atomic positions of these Al atoms remain poorly resolved. Using silver (Ag) as a molecular probe, this study combines synchrotron X-ray diffraction (SXRD) and high-angle annular dark-field scanning transmission electron microscopy (HAADF-STEM) to reveal the specific locations of Al atoms in ZSM-5, a prototypical zeolite catalyst. Statistical analysis of HAADF-STEM images unambiguously identifies the crystallographic adsorption sites of Ag at T4, T6, and T8, linking their distribution directly to the predominant framework Al sites, which correlates perfectly with the predominant Al sites identified by our previous work. By mapping these Al sites, we establish an atomic-scale model for single atom catalysis within the zeolite framework. This work develops methodologies further to elucidate the structure-activity relationship of industrially relevant zeolite catalysts, providing the foundational knowledge for rationally designing zeolite catalysts with optimised active sites and enhanced performance.

1. Introduction

Zeolites are highly important heterogeneous acid catalysts that have extensive applications in the industrial field. For aluminosilicate zeolites, the replacement of Si^{4+} with Al^{3+} at the tetrahedral sites (T-sites) introduces a negative charge in the framework, which is often counterbalanced by a proton, resulting in the formation of Brønsted acid site (BAS) [1–3]. Thus, the precise positioning of BAS is intricately linked to the distribution of Al atoms within the zeolite framework. Since the location and concentration of acid sites can influence the catalytic and physicochemical properties of zeolites. [4,5] The local Al site-selective distribution is essential for understanding the orientation specificity of adsorption and catalytic reactions. More importantly, determining these sites with atomic precision is a critical prerequisite for designing and understanding single-atom catalysis in zeolites.

The distribution of Al in zeolites has been studied for many decades [6–9]. Both practical experiments and theoretical studies have suggested that the distribution of Al across the chemically inequivalent sites is non-random and heavily dependent on synthetic conditions [10], though this relationship remains under-characterised. ZSM-5, a prototypical zeolite catalyst, has attracted significant attention [11]. There are 12 T-sites in the ZSM-5 framework in theory. However, not all of them are equally occupied. In fact, Al atoms preferentially occupy only a few distinct T-sites [12–14].

---

[*] Corresponding author at: Wolfson Catalysis Centre, Department of Chemistry, University of Oxford, Oxford OX1 3QR, United Kingdom.
[**] Corresponding author.
E-mail addresses: p.ho@imperial.ac.uk (P.-L.B. Ho), guangchao.li@polyu.edu.hk (G. Li).

[1] These authors contributed equally to this work

[2] Professor Shik Chi Edman Tsang, deceased May 20, 2025

https://doi.org/10.1016/j.apcata.2026.120846
Received 11 December 2025; Received in revised form 3 February 2026; Accepted 11 February 2026

Thus, understanding the Al site-selective distribution in the zeolite framework is a priority. Over the years, various techniques have been employed to pinpoint the placement of Al atoms within zeolites, including solid-state nuclear magnetic resonance spectroscopy (SSNMR) for H-ZSM-5 [15–18], Fourier transform infrared (FT-IR) for MFI zeolite [19,20], extended X-ray absorption fine structure (EXAFS) for H-type zeolite [21,22], and X-ray emission spectroscopy (XES) [23,24]. More recently, based on the recently developed resonant X-ray powder diffraction (RXPD) method, directly distinguishing the framework Al and Si atoms in zeolites has been attempted by Bokhoven et al. [25]. Additionally, theoretical calculations were also adopted to investigate the Al zoning of zeolites. Previous computational works have shown that the difference in energy between the most and least stable locations of Al is not larger than 12 kcal/mol [26,27]. While powerful, these techniques provide averaged or indirect information, which limits their overall impact. SSNMR and FT-IR complex spectra can be challenging to show precise Al sites in zeolite unit cells. EXAFS and XES lack the spatial resolution for direct atomic visualisation. Recently, combining resonant soft X-ray diffraction (RSXRD) with molecular adsorption techniques, our group has successfully identified the atomic positions of framework aluminium atoms in ZSM-5 zeolite [28].

Electron imaging techniques have also been utilised on zeolites such as scanning transmission electron microscopy (STEM) [29] and Four-Dimensional STEM (4D-STEM) [30]; incoherent Z-contrast and coherent ptychography can lead us to explore fine structures at high spatial resolution. Liu et al. reported the position of extra-framework molybdenum (Mo) sites adsorbed within the straight channel of ZSM-5 [31]. However, site specificity is lost due to the equivalency of overlapping T-sites along the $< 010 >$ zone axis. Their findings show preferential adsorption of metal particles at positions T1/T7, T5/T11, and T2/T8. Additionally, Wei et al.employed a similar technique, utilising organic molecules with their adsorption sites to pinpoint the location of the acid sites within the straight channel of ZSM-5 [32]. A key limitation of this method is its inability to observe adsorption within the sinusoidal channels, the sole conduits to sites such as T4 and T10. This analysis provides unspecific and incomplete crystallographic details, leaving questions about the exact distribution of Al in relation to the pore network, other aluminium locations, and additional framework species.

Herein, by using combined synchrotron X-ray diffraction (SXRD), SSNMR and quantitative high-angle annular dark-field (HAADF)-STEM, we determine the precise atomic-level positions of Al in the ZSM-5 framework. Silver (Ag) was selected as the molecular probe in this study based on two principal advantages. On the one hand, Ag atoms provide strong Z-contrast against the lighter elements (Si, Al) in the zeolite framework, making individual Ag atomic columns visible as bright spots in HAADF-STEM imaging. On the other hand, Ag^+ ions can easily exchange with protons (H^+) in the ZSM-5 via cation exchange. This allows high dispersion and the stabilisation of isolated Ag^+ cations within the zeolite pores or cages, often coordinated to framework oxygen atoms. The HAADF-STEM results directly reveal the positions of Ag within the zeolite framework, thereby pinpointing the locations of the Al T-sites that serve as their anchoring points.

2. Materials and methods

2.1. Catalyst preparation

ZSM-5 was provided by Sinopec, China. Silver nitrate (99 %) was obtained from Sigma-Aldrich. The Si/Al ratio of ZSM-5 was shown to be 17 by inductively coupled plasma-atomic emission spectroscopy (P-4010/ICP-AES). The sample was heated to 753 K under air at a ramp rate of 1 $K{\cdot}min^{-1}$s and calcined for 2 h, then allowed to cool naturally. Ion-exchange was performed by stirring 1.0 g ZSM-5 with silver nitrate solution (0.016 g in 30 mL deionised water) and stirring for 24 h, which formed 1 wt% Ag-ZSM-5. All the procedures were performed using alumina foil-covered vessels to suppress light illumination which can lead to the aggregation of silver atoms to form clusters.

2.2. Structure characterisation

To construct a comprehensive suite of correlated structural characterisation, we used atomic-scale structural data by comparing and combining both averaged and local structural information. The X-ray absorption fine structure data were collected at beamline BL07A of the National Synchrotron Radiation Research Center (NSRRC) in Taiwan. A Si (111) Double Crystal Monochromator (DCM) was used to scan the photon energy. The energy resolution ($\Delta E/E$) in fluorescence mode is approximately 2×10^{-4}, the EXAFS was scanned over the Ag k-edge. IFEFFIT 1 with Horae packages (Athena and Artemis) was used for fitting. The amplitude parameter was set as a fixed input parameter for refinement of the absorber coordination number. High-resolution SXRD data were collected on Beamline I11, Diamond Light Source, UK. The energy of the incident X-ray beam was set at 15 keV. The wavelength and the 2θ-zero-point correction were refined using a diffraction pattern obtained from a high-quality silicon powder (SRM640c). All the catalysts were loaded in a 0.5 mm borosilicate glass capillary. High-resolution XRD data were obtained from the samples using the multi-analyzer crystal (MAC) detectors.

SSNMR measurements were performed to characterise the framework and acid sites. SSNMR spectra were acquired on a JEOL ECZ500R spectrometer (11.7 T, ^1H frequency of 500 MHz) under magic-angle spinning (MAS). ^1H MAS NMR spectra were acquired on a 3.2 mm probe with a spinning rate of 12 kHz, a $\pi/2$ pulse length of 3.05 μs, and a recycle delay of 5 s, while the samples used for the ^1H MAS NMR studies were additionally dehydrated by heating to 673 K at 1 K/min under a dynamic vacuum ($<10^{-3}$ Pa) for 10 h. After cooling to room temperature, the sample tubes were flame sealed. For measurement, the sealed tubes were opened in a nitrogen-filled glovebox, and the samples were packed into ZrO_2 rotors with Kel-F caps. ^{27}Al MAS NMR spectra were acquired on a 3.2 mm probe with a spinning rate of 12 kHz, a pulse length of 0.2 μs ($<\pi/12$), and a recycle delay of 1 s. The 2D ^{27}Al triple-quantum (3Q) MAS NMR experiments were conducted using the 3.2 mm probe with a spinning rate at 12 kHz and pulse length at 0.2 μs ($< \pi/12$). The optimised pulse widths were p1 = 5.0 μs, p2 = 1.4 μs, and p3 = 6 μs. ^{29}Si MAS NMR spectra were acquired on a 8 mm probe with a spinning rate of 4 kHz, a $\pi/2$ pulse length of 5.2 μs, and a recycle delay of 80 s. Unlike the ^1H spectra, the ^{27}Al and ^{29}Si MAS NMR investigations were carried out with samples that were fully hydrated.

The N_2 adsorption–desorption isotherms experiments were performed on a Micromeritics ASAP 2020 micropore analyzer under −196 °C. Samples used in the adsorption measurement were degassed at 300 °C overnight before the measurements. The specific surface area and pore volumes were determined by Brunauer-Emmett-Teller and t-plot methods, respectively.

Zeolites are often sensitive to electron beams, usually withstanding a few thousand electrons per square angstrom under 300 kV STEM conditions [33,34], and recent reports demonstrating ever-increasing resolution [35]. The HAADF-STEM micrographs and associated energy-dispersive X-ray spectroscopy (EDS) analyses were obtained using an aberration-corrected JEOL ARM300F microscope at 300 kV [35] with the annular detector collection semi-angle from 72.80 mrad to 235.75 mrad, the probe array sizes of 1024 × 1024, and a dwell time of 0.3 μs per pixel. Low-dose conditions were used during imaging to avoid amorphous carbon contamination on the beam-sensitive zeolitic framework. Typically, experimental HAADF-STEM imaging conditions of a dose of 13,000 $e^-/Å^2$ are under a probe current of 10 pA, a pixel dwell time of 30 μs, and a pixel size of 0.03 $Å^2$. The combination of experimental and simulated images can further determine whether the contrast of the beam-sensitive zeolite framework is correct. Samples were suspended on a carbon thin film grid. For quantitative EDS mapping and analysis, the sample was analysed at an accelerating voltage of

Table 1
The best-fitted EXAFS data of Ag-ZSM-5.

Scattering path	R-factor: 1.3 %; k-range: 3–10 Å^{-1}; R-range: 1.25–3 Å.		
	Bond length (Å)	Coordination number	Debye-Waller factor
Ag–O1	2.22(3)	3.0(6)	0.015
Ag–O2	2.43(4)	0.8(3)	0.003

200 kV with a live time of ~179 s and a total spectrum count exceeding 380,000 counts, ensuring robust signal statistics and elemental sensitivity. The specimen thickness was estimated to be ~50 nm, suitable for high-fidelity EDX quantification in zeolitic frameworks.

3. Complementary X-ray and electron characterisation of Ag-ZSM-5

3.1. *Modelling derived from SXRD and Rietveld refinement*

The effectiveness of the Ag^{+} exchange was confirmed by ^{1}H MAS NMR spectroscopy (Fig. S1). The spectrum of the pristine H-ZSM-5 exhibited a prominent signal at ~3.9 ppm, attributed to the BAS (Si–O(H)–Al). After Ag^{+} exchange, this signal was drastically diminished, indicating that most protons associated with framework Al have been replaced by Ag^{+} ions [36]. To distinguish between atomically dispersed Ag^{+} cations and metallic Ag clusters, the oxidation state of Ag and local coordination environment in the Ag-ZSM-5 sample were first investigated by X-ray absorption spectroscopy (XAS). The X-ray absorption near edge structure (XANES) spectrum (Fig. S2) exhibited feature characteristic of Ag^{+} ions, providing direct evidence for the monovalent oxidation state of silver and ruling out the presence of Ag^{0}. Subsequently, EXAFS analysis was employed to probe the local coordination environment [37,38]. The quantitative fitting results (Table 1 and Fig. S3) unambiguously confirm the presence of only Ag–O scattering paths. The first shell, Ag–O1, is characterised by a bond length of 2.22(3) Å and a coordination number of 3.0(6). A second, longer Ag–O2 path is also identified, with a bond length of 2.43(4) Å and a lower coordination number of 0.8(3). The observed Ag–O signals are best interpreted as a linear combination of contributions from Ag occupying different sites and their decomposition into site-specific signals is not feasible. Critically, the EXAFS spectra show no evidence of a peak corresponding to an Ag–Ag scattering path (expected at ~2.86 Å for metallic Ag) [39]. This absence definitively confirms the isolated nature of the Ag species. Thus, the combined XANES and EXAFS results conclusively demonstrate that silver exists solely as isolated Ag^{+} cations coordinated to the zeolite framework.

^{27}Al MAS and 3QMAS NMR spectra (Figs. S4a and S5) collectively demonstrated that aluminum existed exclusively as tetrahedral framework species, with no detectable extra-framework Al (EFAl) [40]. This conclusion is corroborated by the ^{29}Si MAS NMR data (Fig. S4b), which showed a Si(0Al) dominated profile (-110 ppm) [41], indicating that the framework aluminum atoms were well isolated. Thereby, a well-defined and phase-pure MFI framework is ensured for the subsequent structural analysis. With this established, we turned to SXRD to determine the precise crystallographic locations of the isolated Ag^{+} sites within the

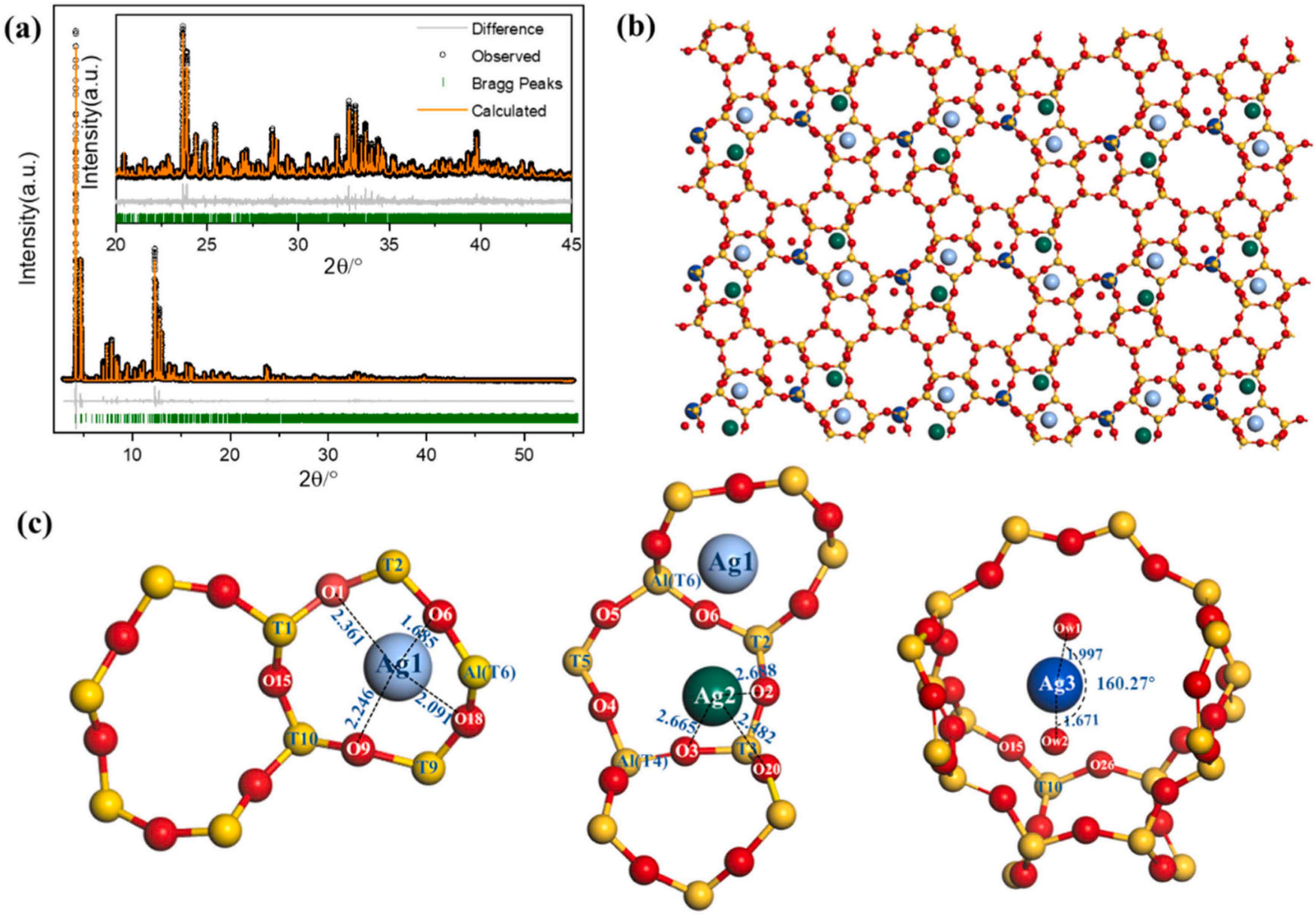

Fig. 1. SXRD characterisation of Ag-ZSM-5 (Si/Al = 20). (a) Rietveld refinement profiles of SXRD data (λ = 0.825868(2) Å, R_{wp} = 7.201 %, Rexp = 3.306 %, GoF = 2.178) for Ag-ZSM-5. (b) Zeolite structure showing the determined Ag sites (Ag1, Ag2, and Ag3) from SXRD. (c) Local zeolite geometry of Ag sites with the bond length information (in Å).

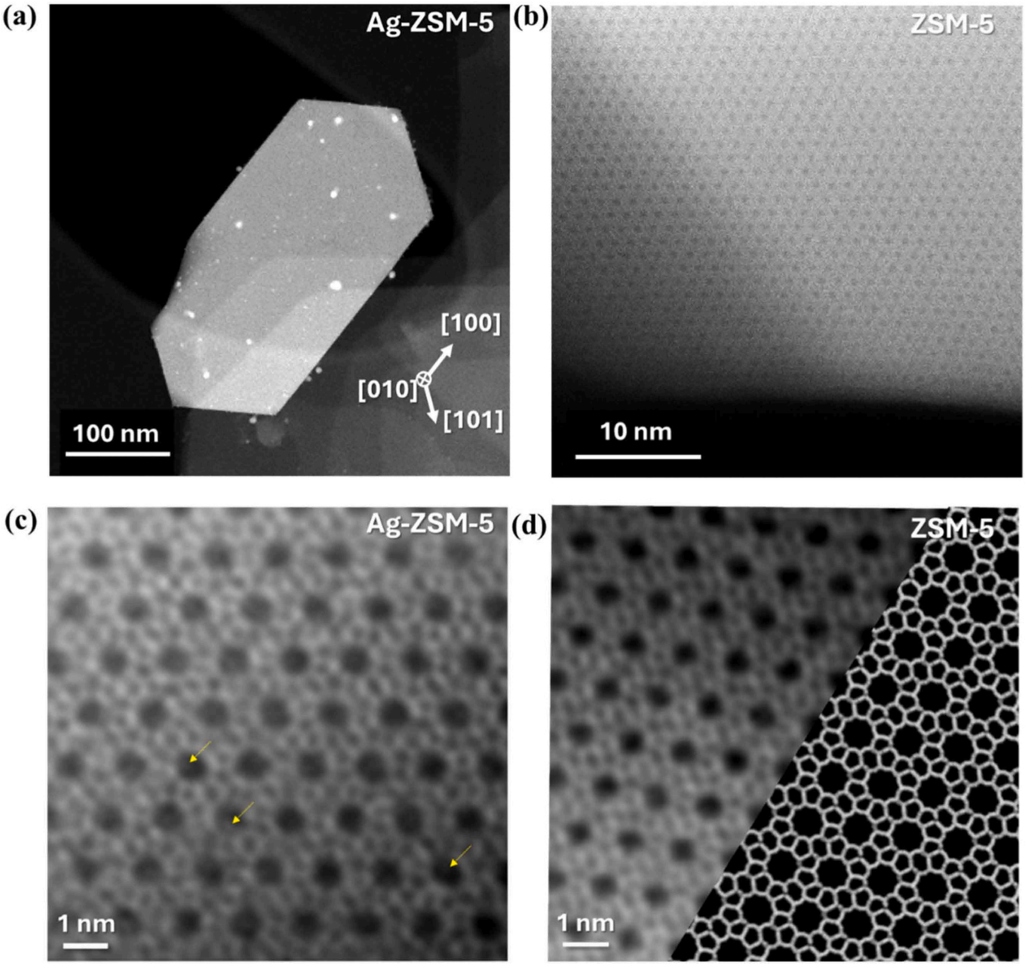

Fig. 2. HAADF-STEM images of pristine ZSM-5 and Ag-ZSM-5 along the [010] zone axis. (a) A low-magnification (60,000x) image showing an elongated, coffin-shaped zeolite crystal. (b) A high-magnification (6 Mx) image of pristine ZSM-5, revealing a clean framework structure. (c) HAADF-STEM (>10 Mx) image of 1 wt% Ag-ZSM-5, where yellow arrows indicate the locations of Ag species. (d) A corresponding image of pristine ZSM-5 for direct comparison.

ZSM-5 channels via Rietveld refinement [42,43]. For accurate analysis, the structure of pristine ZSM-5 was first refined as a reference (Fig. S6). Within the Ag-ZSM-5 channels, the refinement (Fig. 1a) revealed that there are three distinct types of Ag sites (Fig. 1b). The refined structure exhibited reasonable refined parameters with an overall low residual value (Table S1-S3). Furthermore, the average coordination numbers and bond distances show excellent agreement with those obtained from EXAFS.

As shown in Fig. 1c, the Ag1 site is identified as a dehydrated Ag^+ ion positioned on a 5-membered ring at the channel intersection, with an occupancy of 0.05(1). This location corresponds to a known BAS at the T6 position, consistent with previous study [28], indicating that the Ag^+ cation serves to charge-compensate the framework aluminum at this specific T-site. Ag1 is coordinated to four adjacent framework oxygen atoms: Ag1–O1: 2.361 Å, Ag1–O6: 1.685 Å, Ag1–O9: 2.246 Å and Ag1–O18: 2.091 Å, respectively, and does not associate with any non-framework oxygen (absence of hydrated water or hydroxyl moieties). It is noteworthy that the distance between Ag1–O6 is much less than the average Ag–O distance of 2.33 Å ($\Delta d = -0.66$ Å) inferred from EXAFS. We attribute this to the fact that Ag1 occupies the BAS at the T6 position. While prior work [28] identified this Al site, our analysis now specifies the involved framework oxygen (O6). The O6 bonded to the Al^{3+} at T6 likely possesses a higher electron density (compared to other oxygens at this site), facilitating enhanced electron transfer to the Ag^+ ion. The hybridisation of the d_z^2-s orbitals in Ag^+ is not conducive to higher coordination. This favours a monodentate adsorption configuration at the BAS, in which the framework oxygens adequately coordinate the Ag^+ ion with minimal distortion [44].

In contrast to the strongly bound Ag1 site, Ag2 represents a more loosely adsorbed framework-coordinated species with an occupancy of 0.09(1). It is situated above the T-site and is bonded to three framework oxygens (Ag2–O2: 2.688 Å, Ag2–O3: 2.665 Å, and Ag2–O20: 2.484 Å). Notably, the Ag2–O bonds are considerably longer than typical Ag–O bonds, suggesting a weaker electrostatic interaction with the framework. This observation would be consistent with the presence of a BAS at the T4 position. The combined repulsive interactions from the high charge density at T3 and the adjacent BAS proton displace Ag^+ away from the framework, elongating its bonds. Thus, while the proximity to the T4 BAS may facilitate ion exchange, it ultimately results in a less stable adsorption configuration for Ag2 compared to Ag1.

The Ag3 site is the most prevalent silver species in the structure with an occupancy of 0.13(1). It is identified as a diaqua complex $(Ag(H_2O)_2^+)$ [45] located in the centre of the sinusoidal channel, near its intersection with the straight channel. The complex exhibits a slightly curved geometry, with an O_w1–Ag3–O_w2 angle of 160.27°. This is further evidenced by the two significantly different Ag–O_w bond lengths: Ag3–O_w1: 1.997 Å and Ag3–O_w2: 1.671 Å. This difference suggests an asymmetric bonding environment where one water molecule (O_w2) interacts more strongly with the Ag^+ ion, while the other (O_w1) is held more loosely, likely due to differing hydrogen-bonding interactions with the surrounding zeolite framework.

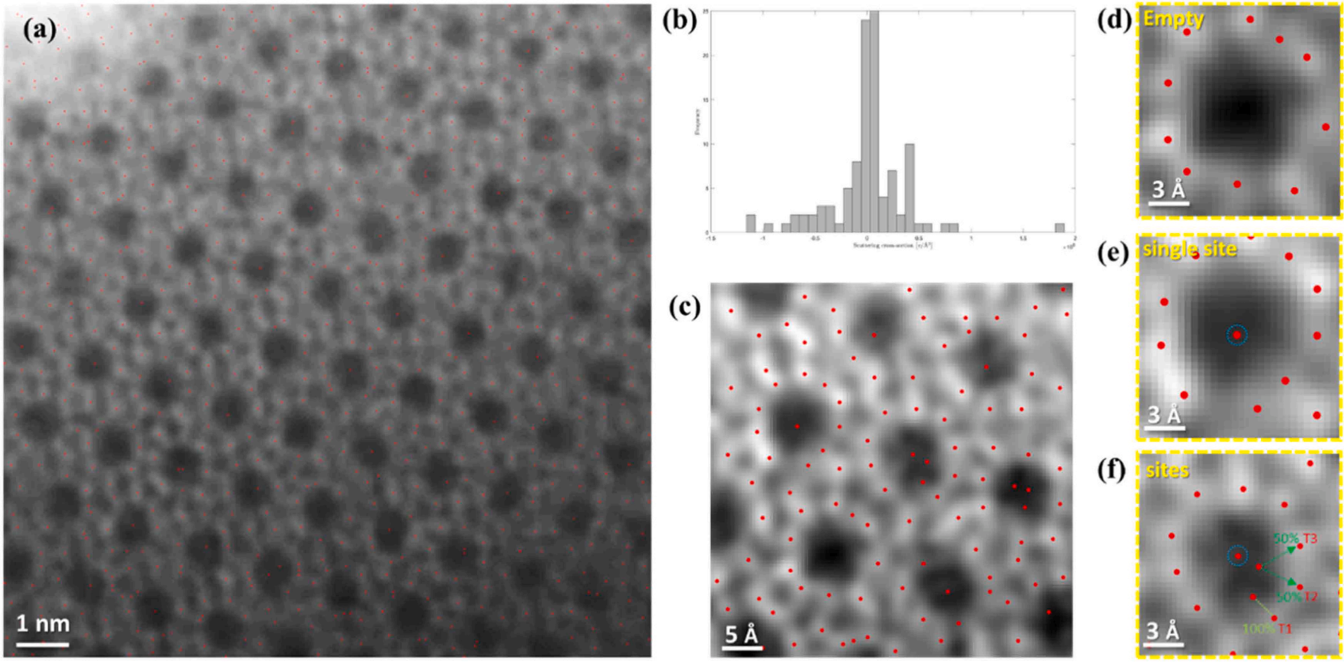

Fig. 3. HAADF-STEM image of 1 wt% Ag-ZSM-5 fitting with Gaussian peak for assignment of Ag. (a) HAADF-STEM image along the [010] zone axis (scale bar: 1 nm), red dots mark the centroids of intensity maxima identified by an automated peak-finding algorithm. (b) Histogram of the scattering cross-section intensity derived from the HAADF-STEM image in (a). (c) Enlarged view of the area in (a) (scale bar: 5 Å). (d-f) Three representative scenarios (scale bars: 3 Å) showing Ag sites identified by automated peak-finding using the threshold from (b): (d) empty (e) 1 site and (f) sites.

3.2. *Direct observation of metal sites by quantitative HAADF-STEM*

HAADF-STEM images at a low magnification of 600,000X show well-facetted ZSM-5 crystals which exhibit the expected coffin-shape (Fig. 2a). Varying and uneven contrast is also observed at the edge area of the image, which can be attributed to thickness differences and the channelling effect due to crystal orientation [46,47]. We also expect additional contrast from the overlap of several plane-shaped crystal particles, and from the carbon grid. The HAADF-STEM contrast shows the clean surface of a pristine ZSM-5 crystal particle (Fig. 2b). The well-defined crystal morphology is consistent with the structural integrity of the framework. N_2 physisorption measurements confirm that the pristine ZSM-5 possesses a high specific surface area (323.9 m^2/g) and a micropore volume of 0.112 cm^3/g, which are characteristic values for a well-crystallised ZSM-5 zeolite. (Fig. S7). It is noted that these edge regions were selected to guarantee that the sample area was thin enough to obtain the atomic-resolved HAADF-STEM images of the Ag-ZSM-5 particle.

To further confirm the crystallographic structure of pristine ZSM-5, the Fast Fourier Transform (FFT) analysis was performed [48,49]. The FFT of the atomic-resolved HAADF-STEM image of pristine ZSM-5 was in good agreement with the simulated electron diffraction pattern of our structure solution from SXRD along the [010] zone axis (Fig S8), thereby conclusively confirming the validity of the structural model. Having validated the structural model, STEM-EDS mapping was employed to verify the chemical homogeneity of the pristine ZSM-5 (Fig. S9). Elemental mapping of Si Kα_1, Al Kα_1, and O Kα_1 clearly reveals a homogeneous distribution of aluminium throughout the pristine ZSM-5 crystal (Fig. S9b-d), the minor Cu signal arises from the TEM support grid (Fig. S9e).

Using low dosage conditions, the contrast in raw HAADF-STEM images limited the determination of the atomic structure of the zeolitic framework (Fig S10). The comparison between original and after-beam-damaged HAADF-STEM images under 300 keV demonstrates the difference of change by incoherent contrast and corresponding FFT as shown in Fig S10. To overcome this question, a nonlinear filtering algorithm can be applied on denoising which is based on Gaussian low-pass filter adding Wiener filter [50]. This nonlinear filtering algorithm could improve the signal-to-noise ratio of the HAADF-STEM images by allowing signals with a frequency below a chosen cutoff frequency to pass through while reducing the strength of signals with frequencies above the cutoff frequency. It is worthwhile to note that the filtering would not change the imaging resolution and add external information besides that in raw HAADF-STEM images. To further confirm that the filtering would not introduce extra artificial aberration, the image simulation is used to cross-analyse the contrast.

Within this established framework, optimised HAADF-STEM imaging was conducted along the [010] zone axis. This viewing direction projects the straight channels and their 10-membered rings (10MRs), allowing Ag metal sites within the channels to be clearly revealed (Fig. 2c). The significant atomic number (Z) contrast between Ag ($Z = 47$) and the framework (Si/Al $Z = 13/14$) makes these sites distinctly visible [51]. This assignment was further verified by a direct comparison with pristine ZSM-5 imaged which was also subjected to the same method, where such high-contrast features are absent (Fig. 2d).

4. Discussion of localisation of Al associated with BAS

Using Gaussian peak fitting (Text S1 and Fig. S11) to determine the local intensity maxima in the direct HAADF-STEM image [52–54], we resolved the locations of Ag adsorption around the 10MRs across 342 straight channels in Ag-ZSM-5 (Fig. 3). The most frequent observation was the absence of a high contrast area within the channels, thus indicating no Ag adsorption (79 channels, 23.1 %), which is reasonable due to the low silver loading of 1 wt%. A total of 263 high contrast sites were observed, which were ascribed to Ag adsorption either over a T-site (61.6 %) or over an O-site (38.4 %).

The analysis of these sites must consider the inherent limitation of the [010] projection, wherein the overlap of crystallographically distinct sites along the b-axis makes them appear equivalent [55,56]. Specifically, each atomic column of T-sites contains two T-sites that alternate along the *b*-axis: the expected site, and its counterpart located

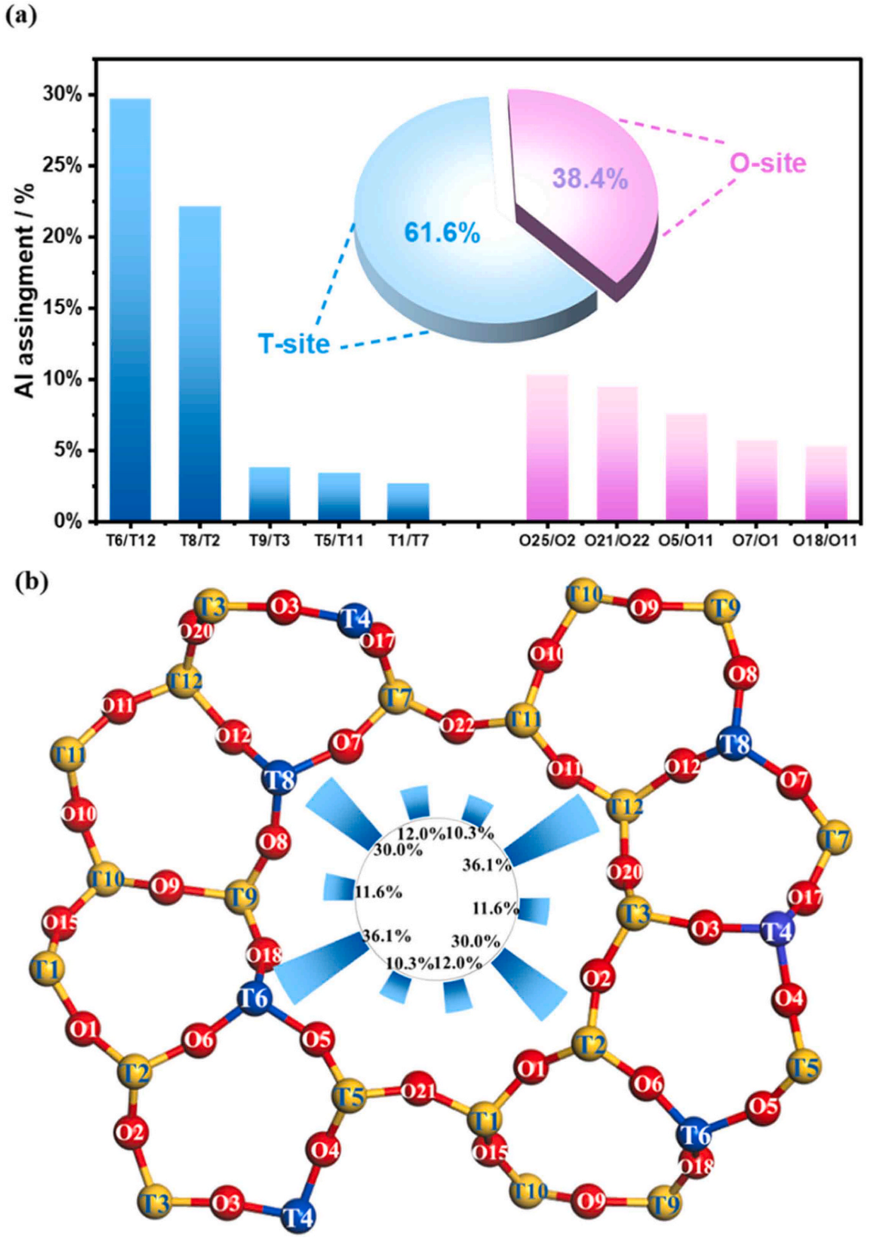

Fig. 4. (a) Al assignment in T-site pairs and O-site pairs; (b) Radial representation of Al assignment with the structural representation overlaid. Al sites as derived by SXRPD show in blue.

diametrically opposite across the straight channel pore (T1/T7, T5/T11, T6/T12, T8/T2, and T9/T3). Hence in our analysis of Al distribution, the Al occupancy is assumed to be statistical within the column, i.e, equally split between the two sites. A similar overlap also affects some O-site columns; therefore, we adopt the terms 'T-site pairs'and 'O-site pairs' throughout this analysis. It is important to note that this static structural model provides a foundational map of acid sites, which under catalytic conditions may dynamically reconfigure [57,58].

The most frequent positions for Ag were observed over T6/T12 (29.7 %) and T8/T2 (22.1 %) (Fig. 4a). Adsorption of Ag at other T-site pairs such as T9/T3, T5/T11, and T1/T7 was observed at much lower frequency (3.8 %, 3.4 %, and 2.7 %, respectively). Significant Ag adsorption was also identified on several oxygen site pairs, with occupancies of 10.3 % for O25/O2 (bridging between T8-T9/T2-T3, respectively), 9.5 % for O21/O22 (between T1-T5/T7-T11, respectively), along with lower occupancies of 7.6 %, 5.7 % and 5.3 % for the O5/O11, O7/O1, and O18/O11 pairs, respectively. The presence of Ag near a T-site is interpreted as bi/tridentate O–Ag–O adsorption, and the central T-site is assigned as an Al site. Meanwhile, Ag adsorption over an O-site is linked to monodentate Ag–O adsorption, in which an adjacent T-site is assigned Al occupancy. As the experimental data does not specify which adjacent T-site bears the aluminium, the occupancy is split equally between both neighbours, purely as a statistical device (blue in Fig. 4b). After redistributing the O-site occupancies, the refined Al distribution remains dominated by T6/T12 (36.1 %) and T8/T2 (30.0 %), followed by T1/T7 (12.0 %), T9/T3 (11.6 %), and T5/T11 (10.3 %).

The significant adsorption at T6/T12 and T8/T2 pairs agrees with our previous investigation of Al distribution on ZSM-5 using soft X-ray resonance powder diffraction (SXRPD), which identified T4, T6 and T8 as the predominant Al sites (Fig. S12) [28]. Furthermore, the consistently low Ag adsorption on the T9/T3, T5/T11, and T1/T7 pairs suggests a low probability of Al occupancy at these specific T-sites. Guided by Löwenstein's Rule that prohibits Al–O–Al linkages [59–61], the Al cannot be located on adjacent T-sites. As all these low-probability T-sites form a cluster sharing corners with T4, we can infer that the Al is predominantly located at the central T4 position. This central conclusion is that Ag adsorption is exclusively dictated by framework Al sites, which is robustly confirmed by the strong correlation between the Ag adsorption map and the aluminum distribution independently determined by SXRPD (Fig. 4b).

It is important to emphasise that the observed preference for Al occupancy at the T4, T6, and T8 sites is specific to the ZSM-5 samples synthesised under the conditions described in this work. The distribution of framework Al is well-known to be influenced by synthesis parameters. Therefore, the primary contribution of this study is not to propose a universal Al siting rule, but to establish and validate a methodology combining Ag^+ probing, SXRD, and HAADF-STEM that can determine site-specific Al distributions with atomic precision.

5. Conclusions

This work directly visualises the predominant framework Al sites by employing Ag as a molecular probe and correlating SXRD with atomic-resolution HAADF-STEM imaging. SXRD refinement identifies three Ag sites in Ag-ZSM-5: a dehydrated Ag^+ (Ag1) at the T6 BAS with a short Ag–O6 bond (1.67 Å), a loosely-bound Ag^+ (Ag2) and a channel-centred $Ag(H_2O)_2^+$ (Ag3). This analysis precisely resolves the crystallographic binding geometries of distinct silver species. Statistical analysis of HAADF-STEM imaging, combined with structural constraints (e.g., Löwenstein's Rule), enables the direct quantification of Al distribution. This analysis establishes a predominance of Al in three T-site pairs: T6/T12, T8/T2, and T4/T10. Such insights provide a deeper atomic-level understanding of the adsorption and reaction properties of ZSM-5 zeolite. While the specific Al distribution reported here is characteristic of our synthetic conditions, the methodological approach is universally applicable. The approaches shown here are expected to be applicable to other types of zeolites and porous crystalline materials, aiding in the better understanding of adsorptive and catalytic processes. By precisely locating these Ag^+ ions, we not only map the underlying Al distribution but also establish a direct structural model for single-atom catalytic sites within the zeolite framework. This approach provides an atomic blueprint that bridges the gap between Al siting and potential catalytic performance, offering a pathway to tailor zeolite catalysts at the single-atom level.

CRediT authorship contribution statement

Yung-Kang Peng: Resources, Formal analysis. **Shik Chi Edman Tsang:** Resources. **Xiting Yue:** Writing – original draft, Visualization, Validation, Methodology, Investigation, Formal analysis. **Tsz-woon Benedict Lo:** Resources, Investigation, Formal analysis. **Wei-Che Lin:** Investigation, Formal analysis. **Tsai-Fu Chung:** Investigation, Formal analysis. **LI Guangchao:** Writing – original draft, Resources, Project administration, Investigation, Funding acquisition, Formal analysis. **Ping-Luen Baron Ho:** Writing – original draft, Visualization, Supervision, Resources, Funding acquisition, Formal analysis, Data curation. **Christopher Foo:** Writing – original draft, Methodology, Investigation, Formal analysis, Data curation.

Declaration of Competing Interest

The authors declare no competing financial interest.

Acknowledgements

P.-L.H would like to acknowledge the Swire Charitable Trust, University College and Mr Raymond Lisheng Liang for his D.Phil. program at Oxford. We thank the final support from the Hong Kong Polytechnic University (PolyU P0049034, P0055259), the Department of Science and Technology of Guangdong Province (GDSTC 2025A1515011688), the Hong Kong Research Grants Council (15301725), the Research Centre for Carbon-Strategic Catalysis (P0058122), the Shenzhen Science and Technology Program (JCYJ20250604185422030), and the National Natural Science Foundation of China (W2541007). We are grateful for the use of characterisation facilities within the David Cockayne Centre for Electron Microscopy, Department of Materials, University of Oxford. The authors thank Christopher S. Allen, Sarah J. Day, Zhiyuan Ding, Peter D. Nellist, Chiu Tang, and Tai-Sing Wu for their valuable discussions and contributions to this work.

Appendix A. Supporting information

Supplementary data associated with this article can be found in the online version at doi:10.1016/j.apcata.2026.120846.

Data Availability

Data will be made available on request.

References

[1] A. Corma, Inorganic solid acids and their use in acid-catalyzed hydrocarbon reactions, Chem. Rev. 95 (1995) 559–614.

[2] J.L. Mancuso, V. Van Speybroeck, The nature of extraframework aluminum species and Brønsted acid site interactions under catalytic operating conditions, J. Catal. 429 (2024) 115211.

[3] X. Wang, C. Wang, Y. Chu, Y. Liu, M. Hu, F. Deng, J. Xu, J. Yu, Deciphering the link between zeolite crystal size, brønsted acid site distribution, and dual-cycle selectivity in methanol-to-olefins over zeolite, ACS Catal. 14 (2024) 15609–15621.

[4] A. Palčić, V. Valtchev, Analysis and control of acid sites in zeolites, Appl. Catal. A Gen. 606 (2020) 117795.

[5] M. Boronat, A. Corma, Factors controlling the acidity of zeolites, Catal. Lett. 145 (2015) 162–172.

[6] Z. Liu, X. Dong, Y. Zhu, A.-H. Emwas, D. Zhang, Q. Tian, Y. Han, Investigating the Influence of mesoporosity in zeolite beta on its catalytic performance for the conversion of methanol to hydrocarbons, ACS Catal. 5 (2015) 5837–5845.

[7] X. Tang, W. Chen, W. Dong, Z. Liu, J. Yuan, H. Xia, X. Yi, A. Zheng, Framework aluminum distribution in ZSM-5 zeolite directed by organic structure-directing agents: a theoretical investigation, Catal. Today 405-406 (2022) 101–110.

[8] G.J. Kennedy, M. Afeworki, S.B. Hong, Probing the non-random aluminum distribution in zeolite merlinoite with ultra-high-field (18.8 T) 27Al and 29, Si MAS NMR Microporous Mesoporous Mater. 52 (2002) 55–59.

[9] D.E. Perea, I. Arslan, J. Liu, Z. Ristanović, L. Kovarik, B.W. Arey, J.A. Lercher, S. R. Bare, B.M. Weckhuysen, Determining the location and nearest neighbours of aluminium in zeolites with atom probe tomography, Nat. Commun. 6 (2015) 7589.

[10] P. Rzepka, T. Huthwelker, J. Dedecek, E. Tabor, M. Bernauer, S. Sklenak, K. Mlekodaj, J.A. van Bokhoven, Aluminum distribution and active site locations in the structures of zeolite ZSM-5 catalysts, Science 388 (2025) 423–428.

[11] Z. Dong, W. Chen, K. Xu, Y. Liu, J. Wu, F. Zhang, Understanding the structure–activity relationships in catalytic conversion of polyolefin plastics by zeolite-based catalysts: a critical review, ACS Catal. 12 (2022) 14882–14901.

[12] O.H. Han, C.-S. Kim, S.B. Hong, Direct evidence for the nonrandom nature of Al substitution in zeolite ZSM-5: an investigation by 27Al MAS and MQ MAS NMR, Angew. Chem. Int. Ed. 41 (2002) 469–472.

[13] S. Sklenak, J. Dědeček, C. Li, B. Wichterlová, V. Gábová, M. Sierka, J. Sauer, Aluminum Siting in silicon-rich zeolite frameworks: a combined high-resolution 27Al NMR spectroscopy and quantum mechanics / molecular mechanics study of ZSM-5, Angew. Chem. Int. Ed. 46 (2007) 7286–7289.

[14] E.N. Domoroshchina, R.D. Svetogorov, G.M. Kuz'micheva, G.V. Kravchenko, L. V. Pirutko, A.I. Zhukova, A.N. Utenyshev, K.V. Bozhenko, Al and Ti location in the MFI orthorhombic HZSM-5 framework. DFT calculation and neutron diffraction experiment, J. Mater. Sci. 58 (2023) 3934–3946.

[15] P. Sazama, J. Dědeček, V. Gábová, B. Wichterlová, G. Spoto, S. Bordiga, Effect of aluminium distribution in the framework of ZSM-5 on hydrocarbon transformation. Cracking of 1-butene, J. Catal. 254 (2008) 180–189.

[16] Z.J. Berkson, M.-F. Hsieh, S. Smeets, D. Gajan, A. Lund, A. Lesage, D. Xie, S. I. Zones, L.B. McCusker, C. Baerlocher, B.F. Chmelka, Preferential siting of aluminum heteroatoms in the zeolite catalyst Al-SSZ-70, Angew. Chem. 131 (2019) 6321–6325.

[17] X. Yi, K. Liu, W. Chen, J. Li, S. Xu, C. Li, Y. Xiao, H. Liu, X. Guo, S.-B. Liu, A. Zheng, Origin and structural characteristics of tri-coordinated extra-framework aluminum species in dealuminated zeolites, J. Am. Chem. Soc. 140 (2018) 10764–10774.

[18] K. Muraoka, W. Chaikittisilp, Y. Yanaba, T. Yoshikawa, T. Okubo, Directing aluminum atoms into energetically favorable tetrahedral sites in a zeolite framework by using organic structure-directing agents, Angew. Chem. Int. Ed. 57 (2018) 3742–3746.

[19] L. Lin, A.M. Sheveleva, I. da Silva, C.M.A. Parlett, Z. Tang, Y. Liu, M. Fan, X. Han, J. H. Carter, F. Tuna, E.J.L. McInnes, Y. Cheng, L.L. Daemen, S. Rudić, A.J. Ramirez-Cuesta, C.C. Tang, S. Yang, Quantitative production of butenes from biomass-

derived γ-valerolactone catalysed by hetero-atomic MFI zeolite, Nat. Mater. 19 (2020) 86–93.

[20] G. Sastre, V. Fornes, A. Corma, On the Preferential Location of Al and Proton Siting in Zeolites: A Computational and Infrared Study, J. Phys. Chem. B 106 (2002) 701–708.

[21] J. Jiao, J. Kanellopoulos, B. Behera, Y. Jiang, J. Huang, V.R. Reddy Marthala, S. S. Ray, W. Wang, M. Hunger, Effects of adsorbate molecules on the quadrupolar interaction of framework aluminum atoms in dehydrated zeolite H,Na-Y, J. Phys. Chem. B 110 (2006) 13812–13818.

[22] A. Vjunov, J.L. Fulton, T. Huthwelker, S. Pin, D. Mei, G.K. Schenter, N. Govind, D. M. Camaioni, J.Z. Hu, J.A. Lercher, Quantitatively probing the Al distribution in zeolites, J. Am. Chem. Soc. 136 (2014) 8296–8306.

[23] K. Gołąbek, E. Tabor, V. Pashkova, J. Dedecek, K. Tarach, K. Góra-Marek, The proximity of aluminium atoms influences the reaction pathway of ethanol transformation over zeolite ZSM-5, Commun. Chem. 3 (2020) 25.

[24] R. Bohinc, J. Hoszowska, J.-C. Dousse, W. Błachucki, F. Zeeshan, Y. Kayser, M. Nachtegaal, A.B. Pinar, J.A. van Bokhoven, Distribution of aluminum over different T-sites in ferrierite zeolites studied with aluminum valence to core X-ray emission spectroscopy 19 (2017) 29271–29277.

[25] A.B. Pinar, P. Rzepka, A.J. Knorpp, L.B. McCusker, C. Baerlocher, T. Huthwelker, J. A. van Bokhoven, Pinpointing and quantifying the aluminum distribution in zeolite catalysts using anomalous scattering at the Al absorption edge, J. Am. Chem. Soc. 143 (2021) 17926–17930.

[26] K.-P. Schröder, J. Sauer, M. Leslie, C.R.A. Catlow, Siting of AI and bridging hydroxyl groups in ZSM-5: a computer simulation study, Zeolites 12 (1992) 20–23.

[27] J.G. Fripiat, F. Berger-André, J.-M. André, E.G. Derouanc, Non-empirical quantum mechanical calculations on pentasil-type zeolites, Zeolites 3 (1983) 306–310.

[28] G. Li, C. Foo, R. Fan, M. Zheng, Q. Wang, Y. Chu, J. Li, S. Day, P. Steadman, C. Tang, T.W.B. Lo, F. Deng, S.C.E. Tsang, Atomic locations and adsorbate interactions of Al single and pair sites in H-ZSM-5 zeolite, Science 387 (2025) 388–393.

[29] P.-L. Ho, C. Foo, W.-C. Lin, S.C.E. Tsang, P.D. Nellist, Spatial differentiation of aluminium siting by the single-atom adsorption sites in zeolite by electron microscopy, Microsc. Microanal. 28 (2022) 2156–2158.

[30] H. Sha, J. Cui, J. Li, Y. Zhang, W. Yang, Y. Li, R. Yu, Ptychographic measurements of varying size and shape along zeolite channels, Sci. Adv. 9 (2023) eadf1151.

[31] L. Liu, N. Wang, C. Zhu, X. Liu, Y. Zhu, P. Guo, L. Alfilfil, X. Dong, D. Zhang, Y. Han, Direct imaging of atomically dispersed molybdenum that enables location of aluminum in the framework of zeolite ZSM-5, Angew. Chem. Int. Ed. 59 (2020) 819–825.

[32] B. Shen, H. Wang, H. Xiong, X. Chen, E.G.T. Bosch, I. Lazić, W. Qian, F. Wei, Atomic imaging of zeolite-confined single molecules by electron microscopy, Nature 607 (2022) 703–707.

[33] X. Li, J. Wang, X. Liu, L. Liu, D. Cha, X. Zheng, A.A. Yousef, K. Song, Y. Zhu, D. Zhang, Y. Han, Direct imaging of tunable crystal surface structures of MOF MIL-101 using high-resolution electron microscopy, J. Am. Chem. Soc. 141 (2019) 12021–12028.

[34] A. Liutkova, V. Drozhzhin, J.M.J.J. Heinrichs, V. Jestl, A. Evtushkova, B. Mezari, Á. Mayoral, N. Kosinov, E.J.M. Hensen, Role of strontium cations in ZSM-5 zeolite in the methanol-to-hydrocarbons reaction, J. Phys. Chem. Lett. 14 (2023) 6506–6512.

[35] C.M. O'Leary, C.S. Allen, C. Huang, J.S. Kim, E. Liberti, P.D. Nellist, A.I. Kirkland, Phase reconstruction using fast binary 4D STEM data, Appl. Phys. Lett. 116 (2020).

[36] Y. Sun, L. Liang, M. Yang, Y. Ji, G. Hou, K. Chen, Identification and quantification of Al pairs and their impact on dealumination in zeolites, J. Am. Chem. Soc. 147 (2025) 10160–10171.

[37] Y. Yang, Y. Xiao, L. Jiang, J. Li, J. Li, J. Jia, C.T. Yavuz, F. Cui, X. Jing, G. Zhu, Ultrahigh single Au atoms loaded porous aromatic frameworks for enhanced photocatalytic hydrogen evolution, Adv. Mater. 36 (2024) 2404791.

[38] R. Jena, V. Kashyap, R. Jana, T. Mandal, T.N. Das, F.A. Rahimi, S. Barman, D. Maity, R. Kumar, D. Bhattacharyya, A. Datta, T.K. Maji, In situ tracking of Ni-MOF reconstruction into active $Ni(OH)_2$ OER catalysts, Angew. Chem. Int. Ed. 64 (2025) e202510741.

[39] N.J. Firet, M.A. Blommaert, T. Burdyny, A. Venugopal, D. Bohra, A. Longo, W. A. Smith, Operando EXAFS study reveals presence of oxygen in oxide-derived silver catalysts for electrochemical CO_2 reduction, J. Mater. Chem. A 7 (2019) 2597–2607.

[40] Y. Ni, X. Gong, W. Zhang, H. Li, Y. Sheng, S. Xu, Y. Wei, W. Zhu, Z. Liu, Site-specific carbonylation of dimethoxymethane over brønsted acids in the opened sodalite cages of FAU zeolite, J. Am. Chem. Soc. 147 (2025) 44950–44961.

[41] J. Dědeček, E. Tabor, S. Sklenak, Tuning the aluminum distribution in zeolites to increase their performance in acid-catalyzed reactions, ChemSusChem 12 (2019) 556–576.

[42] J. Zhang, H. Ding, H. Hui, Q. Yao, W. Feng, T. Chen, T.W.B. Lo, Y. Ren, L. Ye, B. Yue, H. He, Confined Cu single sites in ZSM-5 for photocatalytic hydroxylation of benzene to phenol, Small 20 (2024) 2405150.

[43] G.R. da Silva, G.A. da Silva, J.P.D. Querino, L.G. Possato, Refinement of crystal structure and its application for catalytic materials, Eur. J. Inorg. Chem. 28 (2025) e202500051.

[44] W.-C. Lin, S. Wu, G. Li, P.-L. Ho, Y. Ye, P. Zhao, S. Day, C. Tang, W. Chen, A. Zheng, B.T.W. Lo, S.C. Edman Tsang, Cooperative catalytically active sites for methanol activation by single metal ion-doped H-ZSM-5, Chem. Sci. 12 (2021) 210–219.

[45] M. Busato, A. Melchior, V. Migliorati, A. Colella, I. Persson, G. Mancini, D. Veclani, P. D'Angelo, Elusive coordination of the Ag+ Ion in aqueous solution: evidence for a linear structure, Inorg. Chem. 59 (2020) 17291–17302.

[46] V. Veligura, G. Hlawacek, R. van Gastel, H.J.W. Zandvliet, B. Poelsema, Channeling in helium ion microscopy: mapping of crystal orientation, Beilstein J. Nanotechnol. 3 (2012) 501–506.

[47] G. Li, P.-L.B. Ho, B.K.Y. Ng, T.-S. Wu, P. Rymarz, S.C.E. Tsang, Structural insight into palladium-nickel clusters over mordenite zeolite for carbene-insertion reaction, Front. Chem. Sci. Eng. 18 (2024) 104.

[48] T. Feng, F. Wang, R. Pinal, C. Wassgren, M.T. Carvajal, Investigation of the variability of NIR in-line monitoring of roller compaction process by using fast fourier transform (FFT) Analysis, AAPS PharmSciTech 9 (2008) 419–424.

[49] S.E. Taylor, T. Cao, P.M. Talauliker, J. Lifshitz, Objective morphological quantification of microscopic images using a fast fourier transform (FFT) analysis, Curr. Protoc. Essent. Lab. Tech. 7 (2013) 9.5.1–9.5.12.

[50] H. Du, A nonlinear filtering algorithm for denoising HR(S)TEM micrographs, Ultramicroscopy 151 (2015) 62–67.

[51] S.J. Pennycook, D.E. Jesson, High-resolution *Z*-contrast imaging of crystals, Ultramicroscopy 37 (1991) 14–38.

[52] D. Mukherjee, L. Miao, G. Stone, N. Alem, mpfit: a robust method for fitting atomic resolution images with multiple Gaussian peaks, Adv. Struct. Chem. Imag. 6 (2020) 1.

[53] T. Akkila, T. Lindblad, B. Lund-Jensen, G. Szekely, Å. Eide, A hardware implementation of an analog neural network for Gaussian peak-fitting, Nucl. Instrum. Methods Phys. Res. Sect. A Accel. Spectrometers Detect. Assoc. Equip. 327 (1993) 573–579.

[54] J.-A. Yoon, Y.-H. Kim, N.H. Kim, C.-B. Moon, G. He, W.Y. Kim, Study of energy transfer in single and multi-emissive layer using Gaussian peak fitting, J. Lumin. 153 (2014) 104–108.

[55] J. Holzinger, P. Beato, L.F. Lundegaard, J. Skibsted, Distribution of aluminum over the tetrahedral sites in ZSM-5 zeolites and their evolution after steam treatment, J. Phys. Chem. C. 122 (2018) 15595–15613.

[56] C. Sivadinarayana, V.R. Choudhary, R. Vetrivel, S. Ganapathy, Characterization of silicon sites in monoclinic zeolite ZSM-5 using 29Si magic angle spinning (MAS) nuclear magnetic resonance (NMR) and molecular modelling, Solid State Nucl. Magn. Reson. 13 (1998) 175–182.

[57] G. Li, T. Yoskamtorn, W. Chen, C. Foo, J. Zheng, C. Tang, S. Day, A. Zheng, M.M.-J. Li, S.C.E. Tsang, Thermal alteration in adsorption sites over SAPO-34 zeolite, Angew. Chem. Int. Ed. 61 (2022) e202204500.

[58] J. Li, S.C.E. Tsang, G. Li, Recent advances in heterogeneous frustrated Lewis pair: synthesis, characterization, and catalysis, Adv. Mater. 37 (2025) 2502101.

[59] D. Kiani, S. Sourav, Y. Tang, J. Baltrusaitis, I.E. Wachs, Methane activation by ZSM-5-supported transition metal centers, Chem. Soc. Rev. 50 (2021) 1251–1268.

[60] C.R.A. Catlow, A.R. George, C.M. Freeman, Ab initio and molecular-mechanics studies of aluminosilicate fragments, and the origin of Lowenstein's rule, 1996, pp.1311-1312.

[61] A.V. Larin, The Loewenstein rule: the increase in electron kinetic energy as the reason for instability of Al–O–Al linkage in aluminosilicate zeolites, Phys. Chem. Miner. 40 (2013) 771–780.